JOURNAL OF AIRCRAFT
Vol. 43, No. 6, November–December 2006

Sonic Boom Minimization Using Inverse Design and Probabilistic Acoustic Propagation

Sriram K. Rallabhandi* and Dimitri N. Mavris†
Georgia Institute of Technology, Atlanta, Georgia 30332-0150

DOI: 10.2514/1.20457

Using improved linearized tools that operate on unstructured watertight geometries, the accuracy and efficacy of aerodynamic shape optimization in conceptual design stages can be greatly improved. The conventional area distribution method for minimizing sonic boom is theoretically extended by adding additional parameters so that the near-field signature is more accurately represented. The problem of F-function parameters' estimation is reformulated as a gradient-based optimization problem and solved. Sonic boom propagation is carried out in a probabilistic fashion using parametric atmospheric models and statistical techniques. A bilevel pseudoinverse optimization is performed using coarse-grained parallel genetic algorithms to design aircraft that meet low sonic boom requirements under atmospheric uncertainty. The optimization analysis is split into two cycles with multiple conflicting objectives. Results are presented and discussed.

Nomenclature

A	=	area of ray tube, ft^2
A_e	=	equivalent area, ft^2
A_h	=	area of ray tube at altitude h, ft^2
AD^2	=	Anderson–Darling test statistic
a	=	local speed of sound, ft^2
a_h	=	local speed of sound at altitude h, ft/s
B, B_1, B_2, B_3	=	rise slopes in F-function
$\boldsymbol{b}_1$	=	input layer bias vector
$\boldsymbol{b}_2$	=	output layer bias vector
CV	=	critical value in Anderson–Darling test
F	=	F-function
F_0	=	cumulative distribution function of the assumed distribution
GW	=	gross weight of the aircraft, lb
h	=	cruise altitude, ft
H, C, D, λ, y_r	=	parameters associated with the F-function
l	=	aircraft length, ft
M_h	=	Mach number at cruise altitude h
M_z	=	Mach number at altitude z below cruise altitude
N	=	statistical sample size
p	=	local pressure, psf
pr/pf	=	ratio of rear-to-front shock strength
S	=	slope of balancing line in F-function
S_1	=	heuristic in Anderson–Darling test
U	=	freestream velocity, ft/s
V	=	hidden layer network weights
W	=	output layer network weights
x, y, ξ	=	dummy axial locations
$\boldsymbol{x}_k$	=	vector of known variables
y_f	=	bluntness parameter
y_r	=	intersection of the F-function and the rear balancing line
z	=	vertical distance below cruise altitude
$\alpha_1, \beta_1, \gamma_1, \delta_1, \alpha_2, \beta_2, \gamma_2, \delta_2$	=	dummy variables for equation simplification
α_y	=	nonlinear advance of acoustic rays
β	=	$\sqrt{M^2 - 1}$
ρ	=	local density, slugs/ft^3
ρ_h	=	local density at altitude h, slugs/ft^3
Γ	=	1.2

I. Introduction and Motivation

TRADITIONAL aircraft design process consists of three distinct design phases: conceptual, preliminary, and detailed design. With the ever-increasing computational power, the distinction between conceptual and preliminary design phases is progressively getting blurred. Modern aircraft design requirements impose a significant pressure to conduct advanced multidisciplinary analyses and design from the conceptual phases of design because, at this stage, the design freedom and flexibility are at their maximum. Figure 1 from Mavris and Delaurentis [1] shows the comparison of design freedom and knowledge available at various stages of design between a traditional framework and a desired future framework. As the design proceeds through various stages, the design space shrinks to eventually become the final design space. To achieve the maximum benefit, the designer has to take advantage of the huge design space upfront to avoid serious and costly alterations in design during the later stages. To analyze the large conceptual space, a thorough analysis procedure must be used, but at the same time consideration has to be given to the computational time to perform such an analysis. It is the belief of the authors that this balance of accuracy and time can be achieved by resorting to improved geometry models and linearized methods in the early phases of design.

According to studies conducted by various researchers [2,3], there is a market for a small aircraft that could travel at supersonic speeds over land. Smaller aircraft not only provide destination flexibility, as they can take off and land at many small airports, but they also allow significant performance flexibility, as they have lower penalties associated with stringent criteria such as sonic boom. This paper demonstrates an improved methodology for designing aircraft to minimize sonic boom loudness as well as improving the cruise performance. To this end, improved computational methods have been developed. These include a novel geometry generation and discretization method [4,5] and calculation of accurate equivalent area due to volume and lift [6] based on watertight geometries. Detailed explanation of these methods is provided in the cited

Received 10 October 2005; revision received 26 January 2006; accepted for publication 29 January 2006.

*Postdoctoral Fellow, Aerospace Systems Design Laboratory, Daniel Guggenheim School of Aerospace Engineering. Member AIAA.

†Boeing Professor of Advanced Aerospace Systems Analysis and Director, Aerospace Systems Design Laboratory, Daniel Guggenheim School of Aerospace Engineering. Associate Fellow AIAA.

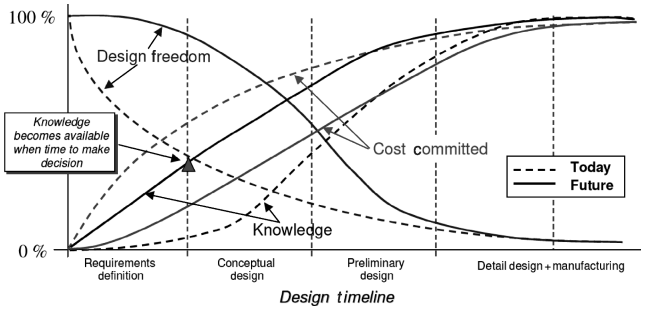

Fig. 1 Different stages of design; adapted from [1].

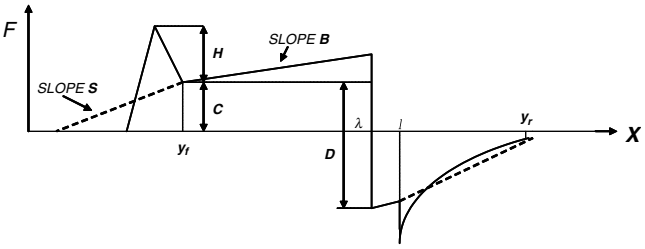

Fig. 2 F-function shape for minimizing pressure rise.

references. The primary focus of this paper is to provide a new architecture of minimizing sonic boom signatures under varying atmospheric conditions using improved linearized methods and inverse optimization techniques.

II. Method for Sonic Boom Minimization

Sonic boom minimization for aircraft design is now being extensively researched at many academic institutions [7,8] and organizations [9,10] and forms the heart of this study. The boom minimization theory of Seebass and George [11] and extension by Darden [12], henceforth referred to as the SGD theory, develops expressions for the near-field signature that minimize shock perturbations. This theory provides low boom constraints that are then used as guidelines to drive the optimizer to achieve those near-field values by changing the shape of the aircraft. Recent research [13] shows that perhaps the most important parameter that should be used for minimization is the loudness level of the pressure signature that is perceived by humans and structures. The existing minimization theory does not provide lower bounds for perceived loudness, rather, it just provides lower bounds for pressure perturbations. Minimizing overpressure or shock pressure rise does not necessarily minimize the perceived loudness, and, therefore, the near-field signature predicted by the existing theory may not yield a signature of minimum loudness. In this section, the SGD theory equations are simplified and recast as a set of two simultaneous equations and an efficient solution strategy is suggested.

In the SGD theory, the coefficients of the F-function [14] are obtained to satisfy certain conditions imposed on the signature. Sonic boom minimization papers in the literature [11,15,16] suggest an F-function that has a Dirac–delta peak at the nose. Darden [12] extended the original F-function representation to the form shown in Eq. (1), to allow for boom–drag tradeoff analysis. The function representing this equation can be sketched as shown in Fig. 2, showing all the relevant parameters.

$$F(y)=\begin{cases}\frac{2yH}{y_f} & 0\le y\le y_f/2\\ C\left(\frac{2y}{y_f}-1\right)-H\left(\frac{2y}{y_f}-2\right) & y_f/2\le y\le y_f\\ B(y-y_f)+C & y_f\le y\le \lambda\\ B(y-y_f)-D & \lambda\le y\le l\end{cases} \tag{1}$$

The relevant equations needed for low boom constraints were derived by Seebass and George [11] and are given in Eqs. (2–7). Equation (2) assumes that the effects due to aircraft wake and engine exhaust can be neglected and that the aircraft volume contribution to equivalent area at the base is zero. Equations (3) and (4) are manifestations of the area balancing rule [14] at the front and rear regions of the F-function. Equation (5) specifies the ratio of the front-to-rear shocks as a function of the desired parameters. This ratio is usually given a value of one. Finally, to ensure that y_r is the intersection of the F-function and the balancing line, Eqs. (6) and (7) are used. These equations are used to solve for H, C, D, λ, and y_r with given values for GW, y_f, p_r/p_f, B, M, h, z, and l and calculated values for G_1, α_y, and S. This produces the required F-function and therefore the equivalent area distribution.

$$A_e(l)=\frac{\beta \mathrm{GW}}{\rho U^2}=4\int_0^l F(y)\sqrt{(l-y)}\,\mathrm{d}y \tag{2}$$

$$\int_0^{y_f} F(y)\,\mathrm{d}y = G_1=\frac{\alpha_y}{2}C \tag{3}$$

$$\int_l^{y_r} F(y)\mathrm{d}y=\frac{-2}{\pi}\int_0^l F(x)\tan^{-1}\left(\sqrt{\frac{y_r-l}{l-x}}\right)\mathrm{d}x=\frac{1}{2}[B(l-y_f) - D + F(y_r)](y_r-l) \tag{4}$$

$$\frac{p_f}{p_r}=\frac{C}{D-B(l-y_f)+F(y_r)} \tag{5}$$

$$F(y_r)=S(y_r-l)+B(l-y_f)-D \tag{6}$$

$$F(y)=-\frac{1}{\pi(y-l)^{1/2}}\int_0^l\frac{(l-\xi)^{1/2}}{(y-\xi)}F(\xi)\mathrm{d}\xi,\qquad y>l \tag{7}$$

Note that a computer program called SEEB exists, based on Darden's paper [12], which calculates the required outputs from the input parameters and flight conditions. However, in the present study, the objective is not only to obtain the F-function that minimizes sonic boom footprint, but also to gain insight into the various terms contributing to the final outputs. This insight could then be used to modify the formulation to make it more generic. The derivation and simplification presented in this paper have not been found elsewhere.

Using the geometric acoustics techniques, closed-form expressions involving integrals can be used to calculate the value of the slope of the balancing line S, as shown in Eq. (8) [17]:

$$S=-\frac{\sqrt{2\beta}}{\Gamma M_h^3\int_0^h\frac{p_h}{p}\sqrt{\frac{\rho a_h}{\rho_h a}}\sqrt{\frac{A_h}{z_h A}}\frac{M}{\beta}\mathrm{d}z} \tag{8}$$

where

$$\frac{A_h}{z_h A}=\left[M_h\sqrt{\left(1-\frac{1}{M_z^2}\right)}\int_0^z\frac{1}{\sqrt{\left(M_z^2-1\right)}}\mathrm{d}z\right]^{-1} \tag{9}$$

The nonlinear advance can be calculated from Eq. (10) by performing numerical integration.

$$\alpha_y=-\frac{\Gamma M_h^3 F(y)}{\sqrt{2\beta}}\int_0^z\frac{p_h}{p}\sqrt{\frac{\rho a_h}{\rho_h a}}\sqrt{\frac{A_h}{z_h A}}\frac{M}{\beta}\mathrm{d}z \tag{10}$$

The slope of the front balancing line S is proportional to the reciprocal of the nonlinear advance at any point of the signal. Therefore, Eq. (8) can also be cast as shown in Eq. (11). Substituting Eq. (6) into Eq. (5) yields an expression for S, which, when considered with Eq. (11), results in an expression for the nonlinear advance at y_f as shown in Eq. (12).

$$S = F(y)/\alpha_y = C/\alpha_{y_f} \tag{11}$$

$$\alpha_{y_f} = (y_r - l)p_r/p_f \tag{12}$$

Using Eqs. (3) and (12), an expression can be obtained for C, as given in Eq. (13), as a function of α_{y_f}, which in turn is a function of y_r.

$$C = \frac{2Hy_f}{(2\alpha_{y_f} - y_f)} \tag{13}$$

Using Eqs. (11) and (13), a quadratic equation in α_{y_f} can be obtained as shown in Eq. (14).

$$2S\alpha_{y_f}^2 - Sy_f\alpha_{y_f} - 2Hy_f = 0 \tag{14}$$

The negative root is extraneous and the positive root is taken to be actual advance, because the advance cannot be negative. The quadratic can be solved for α_{y_f} in terms of y_f, S, and H. The solution is shown in Eq. (15).

$$\alpha_{y_f} = \frac{y_f S + \sqrt{y_f^2 S^2 + 16Hy_f S}}{4S} = (y_r - l)\frac{P_r}{P_f} \tag{15}$$

From Eq. (15), H can be solved in terms of the unknown parameter y_r and is given in Eq. (16).

$$H = \frac{S(y_r - l)^2(P_f/P_r)^2}{y_f} - \frac{S(y_r - l)P_f/P_r}{2} \tag{16}$$

With H and α_{y_f} known in terms of the unknown y_r, Eq. (16) can now be used to obtain C in terms of y_r by substituting in Eq. (13). This is given in Eq. (17).

$$C = \frac{2S(y_r - l)^2(P_f/P_r)^2 - Sy_f(y_r - l)P_f/P_r}{2(y_r - l)(P_f/P_r) - y_f} \tag{17}$$

Following the assumption that the equivalent area contribution due to volume at the base of the aircraft is negligible, the equivalent area due to lift is as given in Eq. (18).

$$A_e(l) = \frac{\beta \mathrm{GW}}{\rho U^2} = 4\int_0^l F(y)\sqrt{(l-y)}\,\mathrm{d}y \tag{18}$$

Because the F-function in Eq. (1) is split into four different intervals, the preceding integral is split into four intervals to carry out the integration. Let $l - \xi = x^2$. The preceding integral reduces to

$$\begin{aligned} A_e(l) = {} & \frac{4H}{y_f}\int_{\sqrt{l}}^{\sqrt{l-\frac{y_f}{2}}} x^2(x^2 - l)\mathrm{d}x + \frac{4C}{y_f}\int_{\sqrt{l-\frac{y_f}{2}}}^{\sqrt{l-y_f}} x^2[4(x^2 - l) \\ & + 2y_f]\mathrm{d}x - \frac{4H}{y_f}\int_{\sqrt{l-\frac{y_f}{2}}}^{\sqrt{l-y_f}} x^2[4(x^2 - l) + 4y_f]\mathrm{d}x \\ & + 4\int_{\sqrt{l-y_f}}^{\sqrt{l-\lambda}} 2x^2[B(x^2 + y_f - l) - C]\mathrm{d}x \\ & + 4\int_{\sqrt{l-\lambda}}^{0} 2x^2[B(x^2 + y_f - l) + D]\mathrm{d}x \end{aligned} \tag{19}$$

The following relations are prescribed to simplify the equations.

$$\beta_1 = \sqrt{l}, \qquad \alpha_1 = \sqrt{l - \frac{y_f}{2}}, \qquad \gamma_1 = \sqrt{l - y_f} \qquad \delta_1 = \sqrt{l - \lambda} \tag{20}$$

Carrying out the integration, the expression for the equivalent area due to lift with the assumed form of the F-function is given in Eq. (21). This equation can then be used to solve for D in terms of y_r and λ and the expression is shown in Eq. (22).

$$\begin{aligned} A_e(l) = {} & \frac{-16H}{y_f}\left[\frac{l}{3}\left(\alpha_1^3 - \beta_1^3\right) - \frac{1}{5}\left(\alpha_1^5 - \beta_1^5\right)\right] \\ & + \frac{4C}{y_f}\left\{\frac{2y_f}{3}\left(\gamma_1^3 - \alpha_1^3\right) - 4\left[\frac{l}{3}\left(\gamma_1^3 - \alpha_1^3\right) - \frac{1}{5}\left(\gamma_1^5 - \alpha_1^5\right)\right]\right\} \\ & - \frac{4H}{y_f}\left\{\frac{4y_f}{3}\left(\gamma_1^3 - \alpha_1^3\right) - 4\left[\frac{l}{3}\left(\gamma_1^3 - \alpha_1^3\right) - \frac{1}{5}\left(\gamma_1^5 - \alpha_1^5\right)\right]\right\} \\ & + 4\left[\frac{2B}{5}\left(\delta_1^5 - \gamma_1^5\right) - \frac{2[B(l - y_f) + C]}{3}\left(\delta_1^3 - \gamma_1^3\right)\right] \\ & + 4\left[\frac{-2B}{5}\delta_1^5 + \frac{2[B(l - y_f) - D]}{3}\delta_1^3\right] \end{aligned} \tag{21}$$

$$\begin{aligned} D = {} & \frac{3}{8(l-\lambda)^{\frac{3}{2}}}\left\{\frac{4(y_r - l)}{y_f}[h1(y_r - l) - h2]A1\right. \\ & \left. + \frac{c1(y_r - l) - c2}{c3(y_r - l) - y_f}(y_r - l)\left(A2 - \frac{8}{3}[(l-\lambda)^{\frac{3}{2}} - k1]\right) - \frac{\beta GW}{\rho U^2}\right\} \end{aligned} \tag{22}$$

where $h1$, $h2$, $A1$, $A2$, $c1$, $c2$, $c3$, and $k1$ are functions of known values and have been clumped together for equation simplification. Similarly, integral Eqs. (4) and (7) can be split into four intervals and integration can be performed. Specifically, Eq. (7) would yield Eq. (23) using the symbols specified in Eq. (20).

$$\begin{aligned} x_p - \tan^{-1}(x_p) = {} & \frac{1}{(2C + 2D)(\sqrt{y_r - l})}\left\{\frac{4H}{y_f}\left[\frac{1}{3}\left(\alpha_1^3 - \beta_1^3\right)\right.\right. \\ & - y_r\left(\sqrt{\alpha_1} - \sqrt{\beta_1}\right) + y_r\sqrt{y_r - l}\left[\tan^{-1}\left(\frac{\alpha_1}{\sqrt{y_r - l}}\right)\right. \\ & \left.\left.\left. - \tan^{-1}\left(\frac{\beta_1}{\sqrt{y_r - l}}\right)\right]\right] + \frac{4C}{y_f}\left[\frac{1}{3}\left(\gamma_1^3 - \alpha_1^3\right) - y_r(\sqrt{\gamma_1} - \sqrt{\alpha_1})\right. \\ & \left.\left. + y_r\sqrt{y_r - l}\left[\tan^{-1}\left(\frac{\gamma_1}{\sqrt{y_r - l}}\right) - \tan^{-1}\left(\frac{\alpha_1}{\sqrt{y_r - l}}\right)\right]\right] \\ & + 2C\left[\left(\sqrt{\gamma_1} - \sqrt{\alpha_1}\right) - \sqrt{y_r - l}\left[\tan^{-1}\left(\frac{\gamma_1}{\sqrt{y_r - l}}\right)\right.\right. \\ & \left.\left. - \tan^{-1}\left(\frac{\alpha_1}{\sqrt{y_r - l}}\right)\right]\right] - \frac{4H}{y_f}\left[\frac{1}{3}\left(\gamma_1^3 - \alpha_1^3\right) - y_r\right. \\ & \left. \times \left(\sqrt{\gamma_1} - \sqrt{\alpha_1}\right) + y_r\sqrt{y_r - l}\left[\tan^{-1}\left(\frac{\gamma_1}{\sqrt{y_r - l}}\right)\right.\right. \\ & \left.\left. - \tan^{-1}\left(\frac{\alpha_1}{\sqrt{y_r - l}}\right)\right]\right] - 4H\left[\left(\sqrt{\gamma_1} - \sqrt{\alpha_1}\right)\right. \\ & \left. - \sqrt{y_r - l}\left[\tan^{-1}\left(\frac{\gamma_1}{\sqrt{y_r - l}}\right) - \tan^{-1}\left(\frac{\alpha_1}{\sqrt{y_r - l}}\right)\right]\right] \\ & + (2By_f - 2C)\sqrt{y_r - l}\left[\tan^{-1}\left(\frac{\sqrt{\gamma_1}}{\sqrt{y_r - l}}\right) - \sqrt{\gamma_1}\right] \\ & + 2B\left[y_r\sqrt{\gamma_1} - \frac{\gamma_1^3}{3} - y_r\sqrt{y_r - l}\tan^{-1}\left(\frac{\sqrt{\gamma_1}}{\sqrt{y_r - l}}\right)\right] \\ & \left. + \pi\sqrt{y_r - l}[S(y_r - l) + B(l - y_f) - D]\right\} \end{aligned} \tag{23}$$

where

$$x_p = \sqrt{\frac{l-\lambda}{y_r - l}} \tag{24}$$

Equation (4) would result in Eq. (26) based on the symbols provided in Eq. (25).

$$\beta_2 = \sqrt{\frac{y_r - l}{l}}, \qquad \alpha_2 = \sqrt{\frac{y_r - l}{l - \frac{y_f}{2}}}, \qquad \gamma_2 = \sqrt{\frac{y_r - l}{l - y_f}}$$
$$\delta_2 = \sqrt{\frac{y_r - l}{l - \lambda}} \tag{25}$$

There are two unknowns, λ and y_r, in two Eqs. (23) and (26). The equations of interest are transcendental equations that are difficult to solve using numerical techniques. Therefore, the equations are recast as an optimization problem such that the squared difference of the right-hand side and left-hand side of Eq. (23) is minimized, whereas Eq. (26) is used as an equality constraint with a tolerance of 10^{-6}. Any change in this tolerance would change the results of the F-function parameters to a certain extent. However, the equality tolerance was not varied during this study. Using λ and y_r, other parameters of the F-function, C, D, and H, can be obtained.

$$\begin{aligned}
&\tan^{-1}\left(\frac{1}{x_p}\right)\left(1 + x_p^2\right) + x_p = \frac{1}{(C+D)(y_r - l)} \\
&\times \left\{\frac{4H(y_r - l)}{y_f}\left(\frac{l}{2}\left[\tan^{-1}(\beta_2)\left(1 + \frac{1}{\beta_2^2}\right) + \frac{1}{\beta_2} - \tan^{-1}(\alpha_2)\right.\right.\right. \\
&\times \left(1 + \frac{1}{\alpha_2^2}\right) - \frac{1}{\alpha_2}\Bigg] - \frac{(y_r - l)}{4}\left[\tan^{-1}(\alpha_2)\left(1 - \frac{1}{\alpha_2^4}\right)\right. \\
&+ \frac{1}{\alpha_2}\left(1 - \frac{1}{3\alpha_2^2}\right) - \tan^{-1}(\beta_2)\left(1 - \frac{1}{\beta_2^4}\right) - \frac{1}{\beta_2}\left(1 - \frac{1}{3\beta_2^2}\right)\Bigg]\Bigg) \\
&+ \frac{C}{y_f}\left[(2l - y_f)(y_r - l)\left[\tan^{-1}(\alpha_2)\left(1 + \frac{1}{\alpha_2^2}\right) + \frac{1}{\alpha_2}\right.\right. \\
&- \tan^{-1}(\gamma_2)\left(1 + \frac{1}{\gamma_2^2}\right) - \frac{1}{\gamma_2}\Bigg] - (y_r - l)(y_r - l) \\
&\times \left[\tan^{-1}(\gamma_2)\left(1 - \frac{1}{\gamma_2^4}\right) + \frac{1}{\gamma_2}\left(1 - \frac{1}{3\gamma_2^2}\right) - \tan^{-1}(\alpha_2)\right. \\
&\times \left.\left.\left(1 - \frac{1}{\alpha_2^4}\right) - \frac{1}{\alpha_2}\left(1 - \frac{1}{3\alpha_2^2}\right)\right]\right] - \frac{H}{y_f}\left[(2l - 2y_f)(y_r - l)\right. \\
&\times \left[\tan^{-1}(\alpha_2)\left(1 + \frac{1}{\alpha_2^2}\right) + \frac{1}{\alpha_2} - \tan^{-1}(\gamma_2)\left(1 + \frac{1}{\gamma_2^2}\right) - \frac{1}{\gamma_2}\right] \\
&- (y_r - l)(y_r - l)\left[\tan^{-1}(\gamma_2)\left(1 - \frac{1}{\gamma_2^4}\right) + \frac{1}{\gamma_2}\left(1 - \frac{1}{3\gamma_2^2}\right)\right. \\
&- \left.\left.\tan^{-1}(\alpha_2)\left(1 - \frac{1}{\alpha_2^4}\right) - \frac{1}{\alpha_2}\left(1 - \frac{1}{3\alpha_2^2}\right)\right]\right] \\
&+ (y_r - l)[B(l - yf) + C]\left[\tan^{-1}(\beta_2)\left(1 + \frac{1}{\beta_2^2}\right) + \frac{1}{\beta_2}\right] \\
&+ \frac{B}{2}(y_r - l)(y_r - l)\left[\tan^{-1}(\gamma_2)\left(1 - \frac{1}{\gamma_2^4}\right) + \frac{1}{\gamma}\left(1 - \frac{1}{3\gamma^2}\right)\right] \\
&- \frac{\pi B}{4}(y_r - l)(y_r - l) - \frac{\pi}{2}(y_r - l)[B(l - y_f) - D] \\
&+ \left.\frac{\pi}{4}(y_r - l)[2B(l - y_f) - 2D + S(y_r - l)]\right\}
\end{aligned} \tag{26}$$

The optimizer used in this exercise is based on sequential quadratic programming (SQP) for constrained optimization. It is a gradient-based optimization [18] procedure which is very efficient for functions which are smooth and have single optimum value. In this case, the functions are indeed smooth and SQP would result in fast convergence. The results of this optimization procedure are shown in Table 1 for a simple case with given input values. Figures 3 and 4 show sample F-function and total equivalent area distributions corresponding to the input values given in this table.

Table 1 Inputs and outputs for a sample run

Variable	Value	F-function parameter outputs	Value
B (slope in F-function)	0.0004	C	0.0496
Mach number	1.6	D	0.1122
Length	130.0 ft	H	0.3480
Gross weight	100000.0 lb	λ	105.92
Altitude	60000.0 ft	y_r	200.89
y_f (bluntness parameter)	10.0		

A. Modifications to the SGD Analysis

The F-function prescribed by Darden [12], used in most conceptual sonic boom minimization studies, can be generalized. In this section, a generalization of the F-function form is given along with the results accompanying such a form. Before proceeding to the derivation of the new set of equations, it is worthwhile to look into some shortcomings of the form prescribed in Eq. (1). The Darden

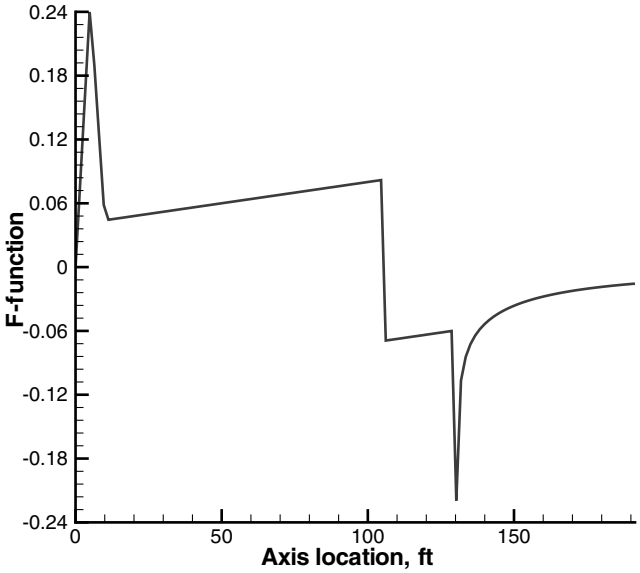

Fig. 3 Sample F-function shape for minimizing pressure perturbations.

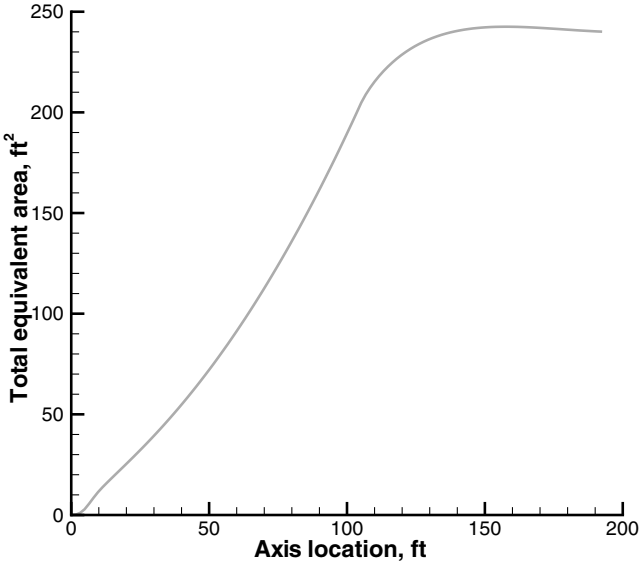

Fig. 4 Sample nonlinear total equivalent area distribution.

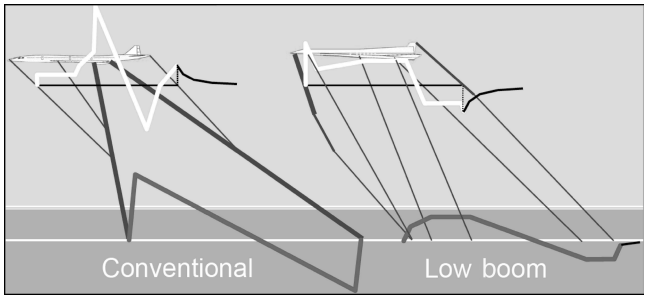

Fig. 5 Pressure signatures of conventional and low sonic boom aircraft [19].

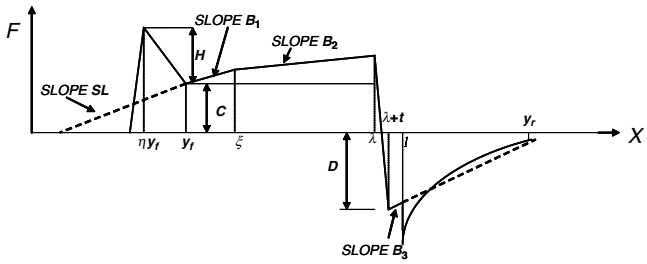

Fig. 6 Proposed description for the F-function.

form assumes that the maximum of the F-function occurs at $y_f/2$. Secondly, the portion after y_f is controlled by just one slope parameter, B. Although this may seem sufficient, consider Fig. 5. This figure [19] qualitatively compares the near-field and far-field pressure signatures of a conventional aircraft and a low boom aircraft. While the left side of the figure produces an N-wave ground pressure signature due to shock coalescence for a conventional aircraft, the right side shows a fairly rounded ground pressure signature with a significantly lower loudness level for a well-designed low sonic boom aircraft. These sort of near-field signatures have been tested by Mack [20]. The near-field pressure signature for the low boom design strategy reveals that improved designs could be achieved by including additional parameters to the SGD F-function. It is with this idea that a generalization of the F-function is introduced with a new form as specified in Eq. (27). Note that this form reduces to the original SGD form for the special case of $\eta = 0.5$, $\xi = y_f$, $B_1 = B_2 = B_3 = B$, and $t = 0.0$. A sketch of the new form is presented in Fig. 6.

$$F(y) = \begin{cases} \frac{yH}{\eta y_f} & 0 \le y \le \eta y_f \\ \frac{C}{(1-\eta)}\left(\frac{y}{y_f} - \eta\right) - \frac{H}{2(1-\eta)}\left(\frac{2y}{y_f} - 2\right) & \eta y_f \le y \le y_f \\ B1(y - y_f) + C & y_f \le y \le \xi \\ B2(y - \xi) + C1 & \xi \le y \le \lambda \\ \frac{-(D+C2)}{t}(y - \lambda) + C2 & \lambda \le y \le \lambda + t \\ B3(y - \lambda - t) - D & \lambda + t \le y \le l \end{cases} \quad (27)$$

Following the analysis procedure carried out earlier, each of the equations derived earlier has a counterpart involving two more variables: ξ and η. Two such counterpart equations are shown in Eqs. (28) and (29), which are expressions for H and C, respectively. Equation (30) specifies the equivalent area distribution corresponding to the minimizing F-function. Further, Eq. (31) has to be satisfied to support the weight of the aircraft in cruise.

$$H = \frac{S(y_r - l)^2(p_r/p_f)^2}{y_f} - \frac{S(1-\eta)(y_r - l)p_r/p_f}{2} \quad (28)$$

$$C = \frac{Hy_f}{(y_r - l)(p_r/p_f) - y_f(1-\eta)} \quad (29)$$

$$\begin{aligned} A_e(x) = {} & \frac{16H}{15\eta y_f}x^{5/2} + 1(x - \eta y_f)\left[\frac{8}{15\eta y_f(1-\eta)}\right. \\ & \left. \times (x - \eta y_f)^{3/2}(2\eta y_f - 2x)\right] + 1(x - y_f)\left[\frac{8}{15y_f}(x - y_f)^{3/2}\right. \\ & \left. \times \left(B_1 yf - \frac{C-H}{1-\eta}\right)(2x - 2y_f)\right] + 1(x - \xi)\left[\frac{8}{15}(x - \xi)^{3/2}\right. \\ & \left. \times (B_2 - B_1)(2x - 2\xi)\right] + 1(x - \lambda)\left[\frac{8}{15}(x - \lambda)^{3/2}\right. \\ & \left. \times \left(B_2 + \frac{D + C_2}{t}\right)(2\lambda - 2x)\right] + 1[x - (\lambda + t)] \\ & \times \left\{\frac{8}{15}(x - \lambda - t)^{3/2}\left(B_3 + \frac{D + C_2}{t}\right)[2x - 2(\lambda + t)]\right\} \end{aligned} \quad (30)$$

$$A_e(l) = \beta \mathrm{GW}/2 = \beta \mathrm{GW}/\rho U^2 \quad (31)$$

Substituting the length for the free variable x in Eq. (30), and using Eq. (31), an equation for D can be obtained as shown in Eq. (32). Equations (33) and (34) are obtained following the same line of derivation as introduced earlier in this paper. The solution is obtained using a numerical optimization approach, as described earlier. This procedure is henceforth referred to as the modified SGD analysis.

$$D = f_1(x_k, \lambda, y_r) \quad (32)$$

$$x_p - \tan^{-1}(x_p) = f_2(x_k, C, D, H, \lambda, y_r) \quad (33)$$

$$\tan^{-1}(1/x_p)\left(1 + x_p^2\right) + x_p = f_3(x_k, C, D, H, \lambda, y_r) \quad (34)$$

The results from the modified SGD analysis have to be compared with the results from the original SGD equations. To simplify the comparison process, the flight conditions are fixed as shown in Table 2. Using the values given in Table 3, new sample F-functions are generated and ground pressure signatures are generated by running PCBOOM [21], which was chosen because of its wide acceptance in the sonic boom community. Figure 7 depicts the changes in the F-function possible while maintaining all the necessary constraints, and Fig. 8 shows the corresponding ground pressure signatures. A few observations can be made from this figure. Firstly, as the axial location of the F-function maximum η gets smaller, the magnitude of the front shock increases. This is because with a lower η, the expansion behind the front shock is not very steep, as in the case where η is large. This lower strength expansion region, during propagation, reduces the strength of the front shock to a lower extent. However, this is accompanied by a reduction in the rear shock

Table 2 Fixed values of some key parameters for a sample run

Variable	Value
M	1.6
l (A/C length)	120.0 ft
GW	120000.0 lb
h (altitude)	60000.0 ft
y_f	25.0

Table 3 Variable values in a sample run comparison

	Original SGD	Modified 1	Modified 2
B_1	2.5×10^{-4}	4.2×10^{-5}	3.9×10^{-5}
B_2	2.5×10^{-4}	1.63×10^{-4}	2.65×10^{-4}
B_3	2.5×10^{-4}	3.26×10^{-4}	2.71×10^{-4}
η	0.5	0.647	0.168
t	0.0	3.367	4.564
ξ	25.0	38.361	36.416

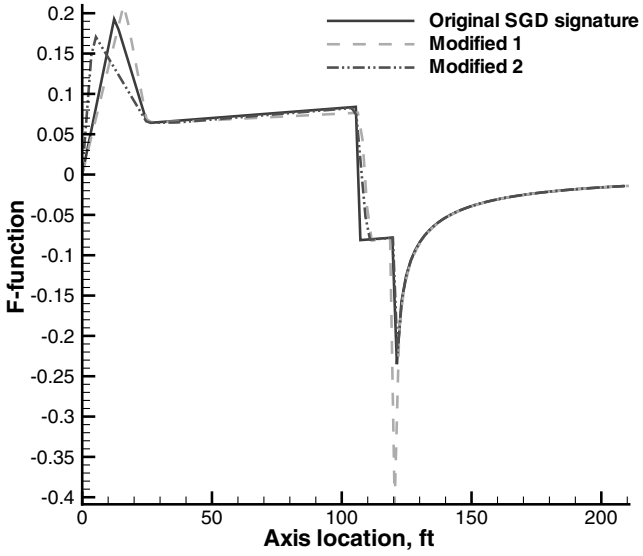

Fig. 7 Modifications to the original SGD F-function.

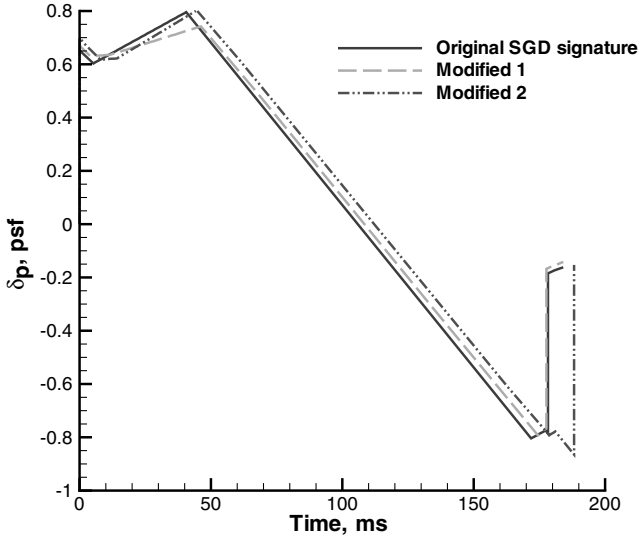

Fig. 8 Corresponding ground pressure signatures.

strength. Secondly, the additional flat regions in the F-function can create a flattoplike pressure signature on the ground. This would not have been possible with the original SGD formulation.

Table 4 shows the important parameters associated with the pressure signature on the ground using the various F-functions. It is clear from the figure and the table that modifications in the F-function could lead to different values of the perceived loudness levels on the ground. Certain variable combinations lead to a reduction in perceived loudness when compared with SGD analysis.

B. Validation of the Modified SGD Analysis Method

Before the modified SGD analyses can be used in the aircraft design and optimization process, they have to be validated against previously known data. Two cases given by Darden [12] are used here for comparison.

1. *Case 1: Minimum Overpressure Solution*

The first case tested is a minimum overpressure solution. This corresponds to the case where the F-function rise slope B is zero. The test case inputs are shown in Table 5. The modified analysis has additional parameters that need to be input. With the additional input values shown in Table 6, the modified SGD analysis is equivalent to the Darden [12] analysis in this case.

Table 4 Comparison of outputs for different F-functions

	Original SGD	Modified 1	Modified 2
PLdB	92.04	92.55	91.90
Shock pressure rise, psf	0.612	0.653	0.659
Overpressure, psf	0.68	0.687	0.802

Table 5 Inputs for test case 1.

Input Variable	Value
M	2.7
l	300 ft
Weight	600000 lb
Altitude	60000 ft
B	0.0
y_f	30.0

Table 6 Additional inputs for modified SGD analysis

Input Variable	Value
B_1	0.0
B_2	0.0
B_3	0.0
η	0.5
t	0.0
ξ	30.0

Table 7 Comparison of the original analysis with modified SGD analyses

Variable	Original Darden [12]	SGD approx.	Modified SGD approx.
H	0.346	0.351	0.347
C	0.0549	0.0553	0.0551
D	0.0683	0.0676	0.0684
λ	270.645	268.118	270.668
Y_r	503.896	505.209	504.237

With the preceding inputs, the modified SGD analysis is run and the outputs are compared in Table 7 with the original Darden [12] results. All the relevant outputs are close to those predicted by Darden. Figure 9 depicts a comparison between the F-functions and Fig. 10 shows the comparison between the equivalent area distributions. The match is almost exact. Another ready check can be

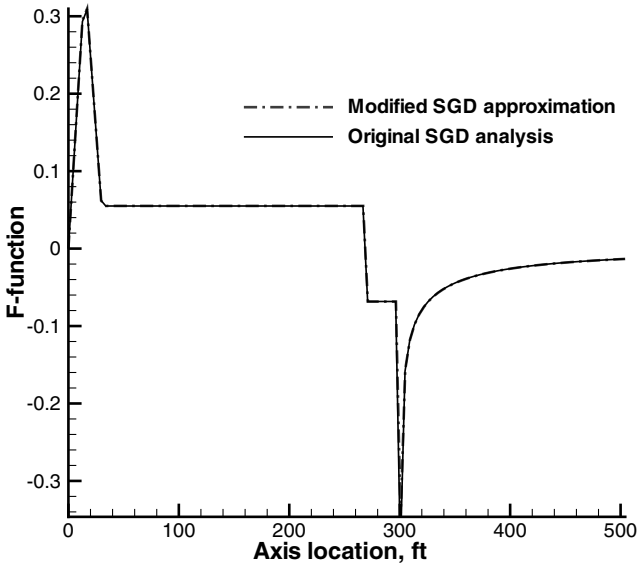

Fig. 9 Comparison of F-functions for case 1.

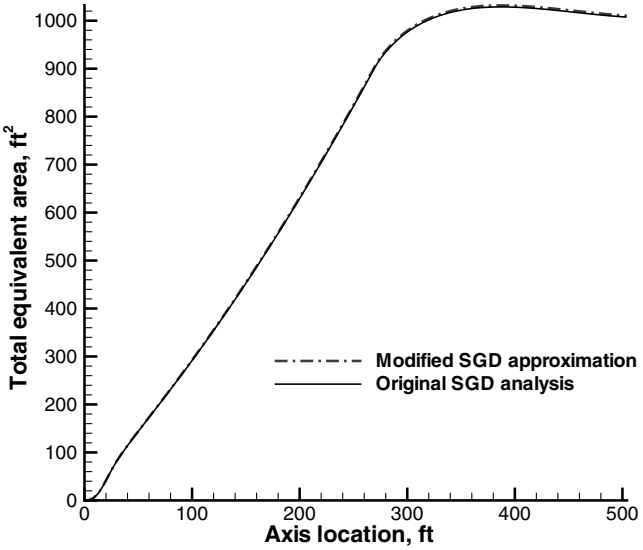

Fig. 10 Comparison of total equivalent areas for case 1.

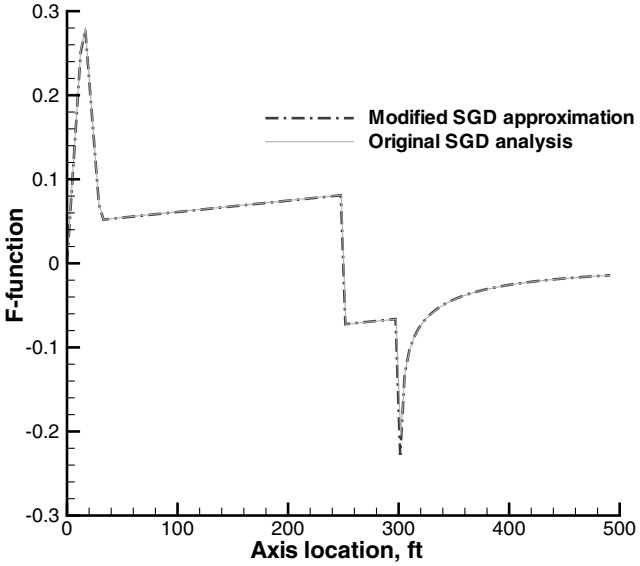

Fig. 11 Comparison of F-functions for case 2.

performed to see if the resultant area distributions actually correspond to the aircraft weight and flight conditions. Based on the relation $A_e(l) = \beta W/\rho V^2$, and the values used in Table 5, a value of approximately 984.17 ft^2 can be obtained for the equivalent area value at the end of the aircraft length. This value is observed in the area distribution plot, thus providing further evidence that the area distributions obtained through optimization are quite close to the actual area distributions.

2. Case 2: Minimum Shock Solution

The next test case is the minimum shock pressure solution suggested by Darden [12]. In this case, all the inputs are the same as before, except now the slope of the rise section in the F-function B is given a value of 1.348310^{-4} instead of zero. This is the value used by Darden in her paper on nose bluntness effect of sonic boom signatures. The resultant outputs are shown in Table 8. It is seen that the outputs from the approximations match almost exactly with the results obtained by Darden. The F-functions and the area distributions obtained from original and modified SGD analyses are compared in Figs. 11 and 12, respectively. An almost identical match is obtained in both the figures.

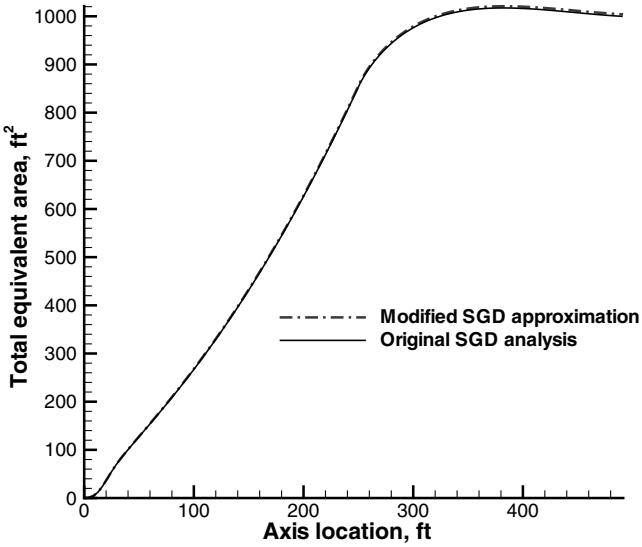

Fig. 12 Comparison of total equivalent areas for case 2.

C. Additional Insights of Modified SGD Analysis

In this section, the effect of the slopes B_i in the modified F-function formulation on the final loudness metrics and pressure signature is examined. Figure 13 depicts a few sample F-functions having varying slope values, keeping most of the other inputs constant. Specifically, Mach = 1.6, length = 120 ft, weight = 120, 000 lb, $y_f = 25.0$, and altitude = 50, 000 ft. The slopes in the sample F-functions have been given arbitrary values equal to positive or negative 0.0003. Figure 14 presents the ground pressure signatures corresponding to the F-functions shown in Fig. 13. Various important conclusions can be deduced following these figures. With all the slopes having negative value, as in case 1, the initial bump in the F-function is larger, to compensate for the expansion in the midregion. Consequently, a larger loudness is associated with this

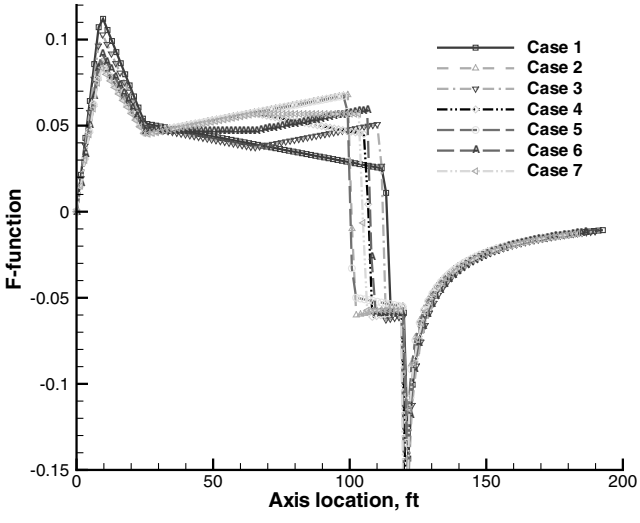

Fig. 13 Sample F-functions with varying slopes.

Table 8 Comparison of the original analysis with modified SGD analyses

Variable	Original Darden [12]	SGD approx.	Modified SGD approx.
H	0.302	0.309	0.303
C	0.0515	0.0520	0.0516
D	0.01021	0.1014	0.1022
λ	251.659	249.139	251.703
Y_r	491.093	493.059	491.452

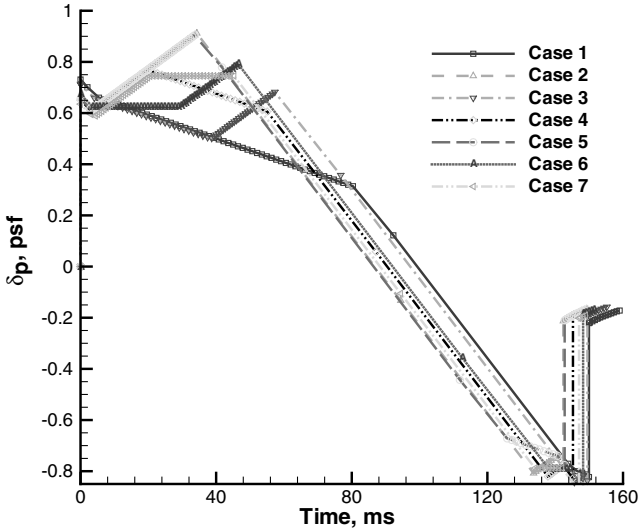

Fig. 14 Sample ground signatures with varying slopes.

signature. By having B_3 go negative while maintaining B_1 and B_2 positive, the front portion of the F-function is not too large in magnitude. However, the rear shock system is reduced in strength, thus leading to a lower loudness value. Cases 2 and 5, with positive values for B_1 and B_2, produce the minimum loudness values. The cases with negative B_1 or negative B_2 produce higher loudness values. Therefore, while performing the optimization studies, it is better to choose positive B_1 and B_2 while B_3 can be allowed to take on positive or negative values. Cases 6 and 7 have been included to show the effect of flat regions in the portion of the F-function after the front shock and expansion. It is observed that a flat region followed by a ramp, as in case 6, produces a stronger front shock than case 7 where the F-function has a ramp followed by a flat region. However, due to the lift constraint, case 7 would have a stronger compression in the midregion, resulting in a higher shock overpressure value. The loudness values and shock perturbations corresponding to these figures are given in Table 9.

Table 9 Effect of varying slopes in F-function

Case	B_1	B_2	B_3	PLdB
1	-3×10^{-4}	-3×10^{-4}	-3×10^{-4}	92.8
2	3×10^{-4}	3×10^{-4}	3×10^{-4}	91.65
3	-3×10^{-4}	3×10^{-4}	3×10^{-4}	93.18
4	3×10^{-4}	-3×10^{-4}	3×10^{-4}	92.0
5	3×10^{-4}	3×10^{-4}	-3×10^{-4}	91.55
6	0.0	3×10^{-4}	0.0	92.5
7	3×10^{-4}	0.0	0.0	92.32

Table 10 Ranges for modified SGD input variables

Variable	Lower bound	Upper bound
$B1$	-3×10^{-4}	4×10^{-4}
$B2$	-3×10^{-4}	4×10^{-4}
$B3$	-3×10^{-4}	4×10^{-4}
Mach number	1.4	1.8
Length	100.0 ft	200.0 ft
Gross weight	80000.0 lb	130000.0 lb
Altitude	40000.0 ft	80000.0 ft
y_f (bluntness parameter)	2.0	30.0
ξ	y_f	$y_f + 40.0$
η	0.2	0.8
t	0.0	5.0

III. Approximate Estimation of Minimum Area Distribution

The procedure laid out in the previous section can be used effectively to estimate the area distributions for minimum boom footprints. However, it has been observed that occasionally the gradient-based optimization terminates prematurely or fails to converge for certain values in the design space. To overcome this problem, an approximation to the modified SGD solution procedure is sought. Points in the design space that lead to fully converged results are used to create an approximation hypersurface of the modified SGD analysis. Because the responses are nonlinear with respect to the inputs, an artificial neural network has been used to aid in the approximation process.

An artificial neural network with a single hidden layer is a universal approximator to any continuous bounded function, provided the right number of neurons are chosen in the hidden layer [22]. For a single hidden layer neural network, the outputs can be specified in terms of the inputs by an equation such as the one shown in Eq. (35), where $\boldsymbol{X}$ and $\boldsymbol{y}$ are the input and output vectors, respectively, and σ represents a nonlinear sigmoidal transfer function, usually with activation 1.0.

$$\boldsymbol{y} = W^T \sigma(V^T \boldsymbol{X} + \boldsymbol{b}_1) + \boldsymbol{b}_2 \tag{35}$$

Supervised networks with batch training are used in this study. Supervised neural networks have two stages. The first is the training stage where the actual analysis is run to record the input–output combinations. This data is then fed to the network, which changes the weight matrices and bias vectors to fit the data in the best possible way. There are various algorithms to fit the data. In this study, a Bayesian regression learning algorithm available in the MATLAB neural network [23] toolbox is used. Once the optimum weight and bias vectors are obtained, the model has to be tested for performance. A test data of input–output pairs is generated using the actual analysis and it is compared with the output from the neural network approximation. If the neural network predicts the test data set satisfactorily, one can assume that the neural network has successfully approximated the analysis function. Training and test data for using the SGD solution procedure have been created with the ranges for the variables provided in Table 10. These ranges were arbitrarily chosen so as to enclose a vast design space for optimization analysis.

A network with 25 hidden layers was chosen. This number was chosen by trial and error to obtain the best possible fit. The number of training and test cases used for the artificial neural network have been chosen with the following logic. Using too many training cases not only increases the computational time, but also causes memorization of the input–response mapping that causes poor generalization for other data. To overcome this difficulty, the 11 dimensional domain was arbitrarily divided into 3 overlapping subdomains: 1) 3 consisting of 7 variables, 2) 1 with 6 variables, and 3) 1 with 4 variables. Within each such subdomain a case was chosen resulting in a total of 464 training cases. The number of test cases was arbitrarily chosen to observe the performance of the neural network approximation over a random sample in the domain. Each of the inputs and outputs has been normalized with respect to the maximum value of particular variables. Figure 15 depicts the normalized training data as well as the output obtained from the neural network. It can be seen from this figure that the neural network was able to successfully track the actual responses by modifying the weights and biases. A good match with training data is only half of the story. The performance of the neural network has to be evaluated with normalized test data. Figure 16 shows the test data and the output from the neural network. It can be seen that the neural network was able to mimic the performance of the actual analysis for most of the test cases. The neural network approximation for the modified SGD analysis can be used as an effective and efficient surrogate to the actual analysis.

IV. Probabilistic Propagation

Noise propagation through the atmosphere is an important element in the estimation of the sonic boom loudness on the ground.

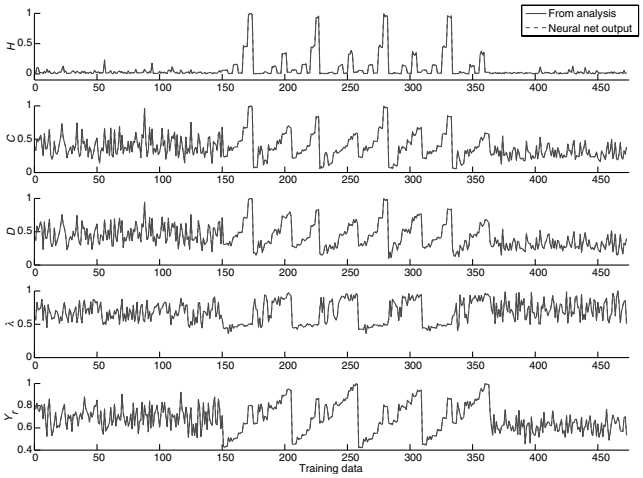

Fig. 15 Neural network training for modified SGD equations.

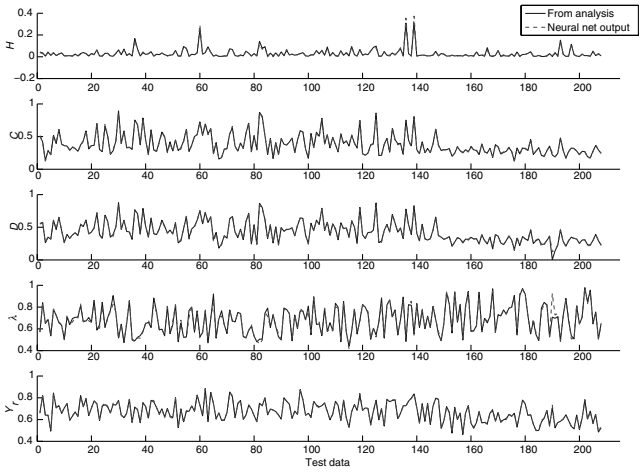

Fig. 16 Neural network testing for modified SGD equations.

Unlike the near-field pressure signature, which is determined by calculating the flowfield around the body, the ground signature is not completely under the control of the designer. This is because the noise amplitude and direction are highly dependent on the prevalent atmospheric conditions. Effects like atmospheric absorption, molecular relaxation [24], turbulence [25], and anomalies in temperature and wind profiles influence the ground pressure signature.

To accurately predict the sonic boom signatures on the ground, models have to be created to capture the atmospheric variations. Creation of higher-fidelity models is an active research topic in the atmospheric science and is beyond the scope of this research. This being a conceptual design study, simple parametric models have been created [6] to capture temperature and wind variations. Because the atmospheric properties are changing over time, location, etc., a deterministic value for sonic boom signatures is inadequate. A simple procedure is described herein to calculate a probabilistic estimate of the shock perturbations and sonic boom loudness when a single near-field signature is propagated through various atmospheric models. Given the area distribution or the F-function, the propagation analysis is run for a fixed number of times with varying temperature and wind profiles. The perceived loudness values for these cases are then used to fit a distribution using the Anderson–Darling test statistic, as explained next.

The Anderson–Darling test [26,27] is one of the most powerful and important goodness-of-fit tests in the statistical literature, especially for small sample sizes. This test is a modification of the Kolmogorov–Smirnov test. It weighs the tails more heavily and uses a hypothesized distribution, resulting in a better goodness-of-fit test. Using the sample points, the parameters of the hypothesized

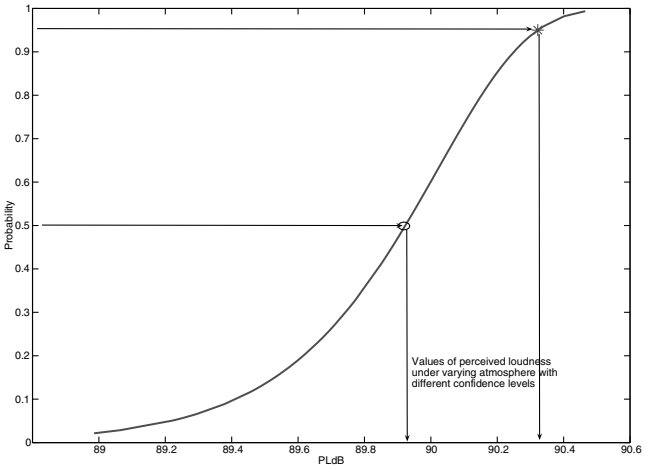

Fig. 17 The perceived loudness level from the cumulative distribution function.

distribution are estimated. Then a critical value of the test statistic corresponding to the hypothesized distribution is determined. Depending on the values of the test statistic and the critical values, the hypothesized distribution is accepted or rejected. The Anderson–Darling test statistic AD^2 is defined in Eqs. (36) and (37) for a normal distribution. In these equations, N is the sample size and F_0 is the cumulative distribution function (CDF) of the assumed distribution.

$$AD^2 = -N - S_1 \tag{36}$$

where

$$S_1 = \sum_{i=1}^{N} \frac{(2i-1)}{N} \{\ell n[F_0(x_i)] + \ell n[1 - F_0(x_{n+1-i})]\} \tag{37}$$

If the mean and variance have to be estimated using the same data used for the test, then the test statistic is modified according to Eq. (38):

$$AD^2 = AD^2 \times \left(1 + \frac{4}{N} + \frac{25}{N^2}\right) \tag{38}$$

The critical value for a normal distribution is given by Eq. (39).

$$CV = 0.75 \Big/ \left(1 + \frac{0.75}{N} + \frac{2.25}{N^2}\right) \tag{39}$$

Now if $AD^2 > CV$, then the hypothesized distribution is rejected as not fitting the sample points. The critical and test statistic values are different for various distributions. In this study, the Anderson–Darling test has been used to accept or reject four possible distributions (normal, log-normal, Weibull, and exponential) due to their frequent occurrence in many statistical studies. After the distribution of the perceived loudness level has been obtained using the Anderson–Darling test, a CDF for that distribution is obtained. A value corresponding to the 95% probable value is then used as the perceived loudness level (PLdB). Figure 17 shows that, depending on the confidence desired by the designer, the perceived loudness value can be obtained from the CDF. The designer could choose the number of samples to use in the Anderson–Darling test. The higher the number of samples, the closer one can get to the actual CDF.

V. Coarse-Grained Parallel Genetic Algorithm

Shape optimization for sonic boom minimization is a multi-objective design problem and is multimodal. This means that various local minima exist in the design space. To add to that, the shape variables consist of discrete and continuous variables. A traditional optimizer like SQP cannot be used for such a problem. Therefore, a genetic algorithm optimizer is used in this study. Genetic algorithms have a few important advantages over gradient-based optimization

Table 11 Variable ranges of parameters for modified SGD optimization

Variable	Lower bound	Upper bound
$B1$	-2×10^{-5}	4×10^{-4}
$B2$	-2×10^{-5}	4×10^{-4}
$B3$	-3×10^{-4}	4×10^{-4}
Mach number	1.45	1.7
Length	100.0 ft	150.0 ft
Gross weight	100000.0 lb	130000.0 lb
Altitude	40000.0 ft	60000.0 ft
y_f (bluntness parameter)	2.0	10.0
ξ	y_f	$y_f + 40.0$
η	0.2	0.5
t	0.0	5.0

schemes. Firstly, they achieve a global optimum instead of getting stuck in a local optimum. Secondly, because they operate on a population of candidates, a Pareto-optimal front can be obtained in a multidimensional space with many conflicting objective functions. Furthermore, because these do not require any gradient information, they can be applied to problems that may be discontinuous. In spite of the advantages mentioned here, genetic algorithms have been the subject of criticism for various reasons. They are computationally very intensive as they lack the elegance of reaching the optimum as in the case of gradient-based optimization. Moreover, as the algorithm continues, some individuals with high fitness values may dominate the population. This causes premature convergence of the population. Premature convergence is avoided in most genetic algorithms by using a technique called niching [28], which tries to include a diverse population after every generation or epoch. The main drawback of slow evolution in conventional genetic algorithms can be overcome by using an efficient parallel implementation of the genetic algorithm that could obtain the results in far less computational time.

Various genetic algorithm parallelization schemes have been proposed [29,30] in the literature. One simple parallel implementation is a coarse-grained genetic algorithm based on the principles of *punctuated equilibria*, *allopatric speciation*, and *stasis*. Any population initially undergoes rapid evolution to new solution. However, as the number of generations increase, the changes to the population are gradual and slow. In that sense, the population attains stability or stasis and could end up in a local optimum. The punctuated equilibrium principle states that in order to continue the evolution to the best population, new population members have to be thrust into the existing population to increase the evolution rate. Allopatric speciation involves the introduction of stabilized individuals into different populations. In this study, a coarse-grained parallel version of a nondominated sorting genetic algorithm (NSGA2) proposed by Deb [31] is developed and used along the parallelization strategy suggested by Gondra and Samadzadeh [29].

VI. Shape Optimization Results

To numerically minimize sonic boom loudness, a pseudoinverse optimization is performed. The analysis is split into two optimization routines. Firstly, using probabilistic propagation techniques, the optimum area distribution, aircraft length, gross weight, Mach number, altitude, and other parameters in the modified SGD analysis that minimize the perceived loudness level on the ground are determined. This optimum distribution is then fed to the next optimization level, where optimum shape parameters, described earlier, are obtained to match the area distribution. The following sections briefly explain these steps and provide the shape optimization results.

A. Optimum Area Distribution

For the sake of conducting an optimization to determine a near-field F-function that reduces the sonic boom loudness, the ranges for the parameters given in Table 11 are considered. The weight is given a minimum value of 100,000 lb, because a lower value is not structurally feasible with the other requirements. Note that these ranges are a subset of the ranges used for the neural network approximation and therefore the artificial neural network can be safely used in lieu of the actual analysis.

The design variables in the optimum area estimation step are the Mach number, gross weight, length, altitude, and other parameters included in the specification of the F-function. Using the neural network approximation, optimum values for these variables are obtained by simultaneously minimizing the probabilistic estimate of the perceived loudness and maximizing the figure of merit [32]. The reason for providing the second conflicting objective is to obtain a Pareto front of area distributions. The best compromised area distribution can then be chosen according to the requirements of the design.

Using the proposed shape optimization technique, a Pareto front of the area distributions is obtained, as shown in Fig. 18. For the purpose of demonstration here, the values and distributions corresponding to the rectangle, PLdB = 84.27, shown in the figure are used as the target values for the second step of the optimization process. The results of the first step are given in Figs. 19 and 20. The resulting F-function has a peak near the nose, followed by a small flat region and

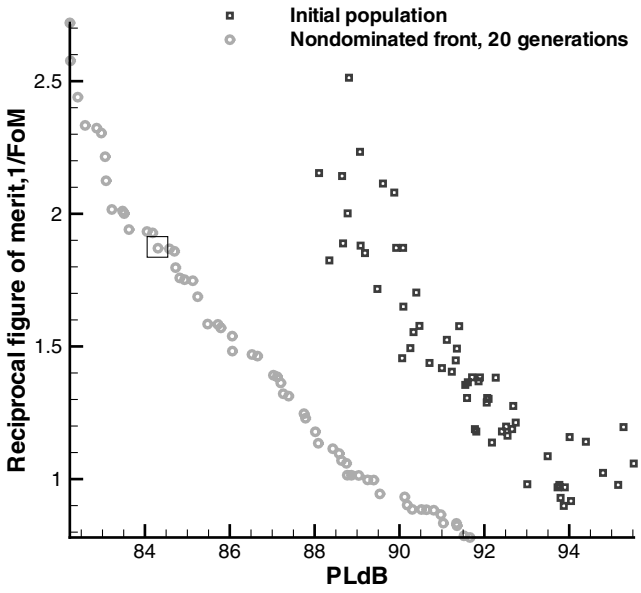

Fig. 18 Pareto front for the first step of optimization.

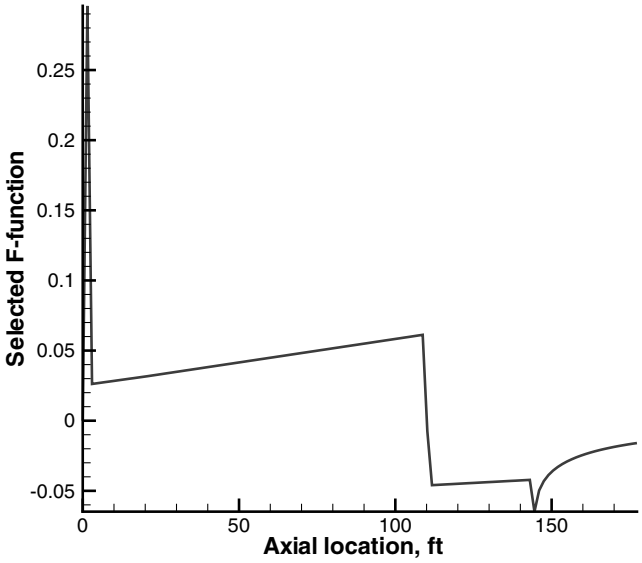

Fig. 19 The optimum F-function chosen from step 1.

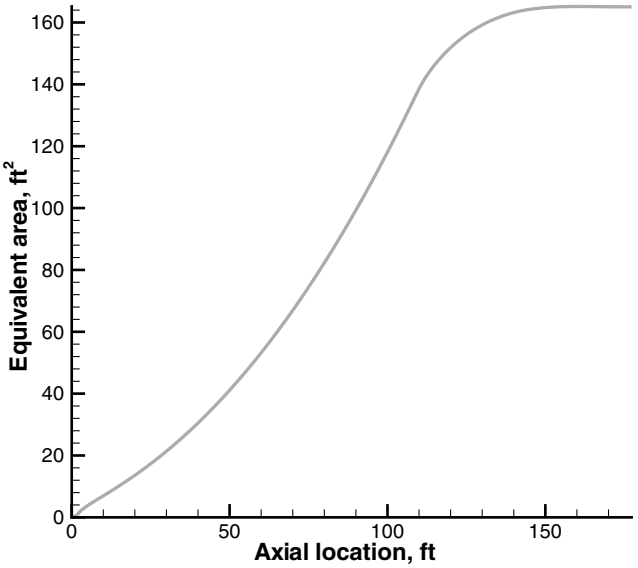

Fig. 20 The target equivalent area distribution chosen for step 2.

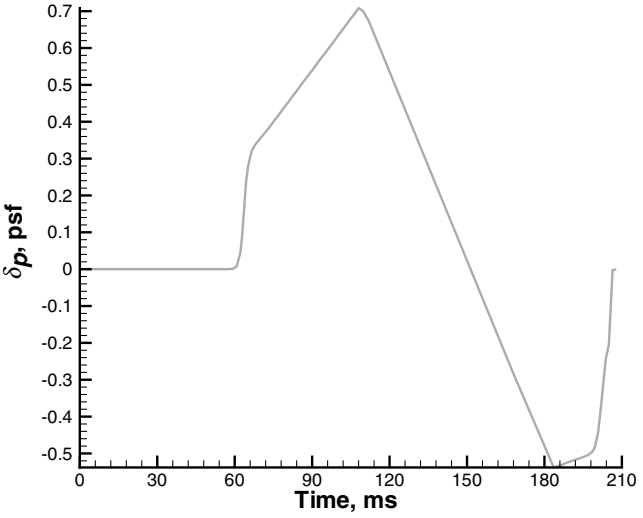

Fig. 21 The ground pressure signature.

a ramp signifying a slow compression. This is then followed by a quick expansion, after which there is a slow expansion. Finally, there is a rear compression to the ambient conditions. Figure 20 depicts the corresponding area distribution, which is used as the target for the second step of optimization. Figure 21 depicts the ground pressure signature corresponding to the highest loudness level when the F-function given in Fig. 19 is propagated through varying atmospheric profiles. As can be seen, the initial shock rise is about 0.242 psf and the maximum overpressure is about 0.7 psf.

For sake of brevity, the results obtained using the original SGD analysis are not shown here. However, it is our observation that, compared with the results from the original SGD analysis, significantly reduced perceived loudness values are obtained by opening up the parametric design space of near-field F-functions. The final optimization values chosen for the second step of optimization are $M = 1.46$, $GW = 102460.76$ lb, altitude= 51660.2 ft, and length = 149.27 ft. Table 12 presents the loudness values corresponding to the preceding ground signature.

B. Estimation of Optimum Aircraft Shape

The next step is the determination of the shape of the aircraft that meets the required area distribution from step 1 without incurring a heavy drag penalty. It has been realized that getting to the target area distribution by varying shape parameters can take a lot of iterations

Table 12 Final loudness values

Loudness metric	Value
PLdB	84.27
dBA, A-weighted loudness level	68.393
dBC, C-weighted loudness level	95.026

and computational time. Using conceptual analysis tools, it may not be possible to achieve an exact match for the equivalent area distribution. Nevertheless, if a close match is obtained, later design stages could use advanced analysis to realize the complete matching of the area distributions. To reduce the computational time, the second step of the optimization process is further split into two steps. In the first step, the fuselage shape is altered to meet the nose shape. Once a suitable match is obtained, the fuselage shape is frozen and the other components are perturbed to reach the final target distribution. By doing this, the problem is decomposed into optimization runs involving lesser numbers of variables.

Figure 22 shows the nondominated population points after 20 generations, along with the initial population for the first substep of the shape estimation process. Figure 23 shows the area match corresponding to a point on the nondominated Pareto front. It can be seen that the nose region is approximated well. With a known nose

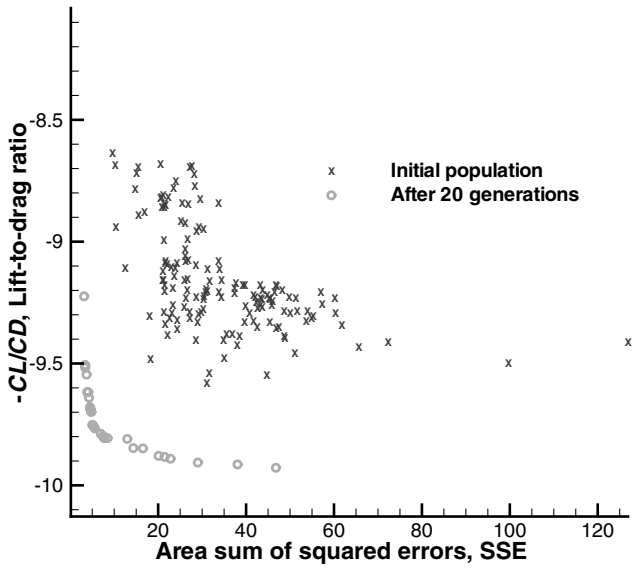

Fig. 22 Pareto front of the nose matching.

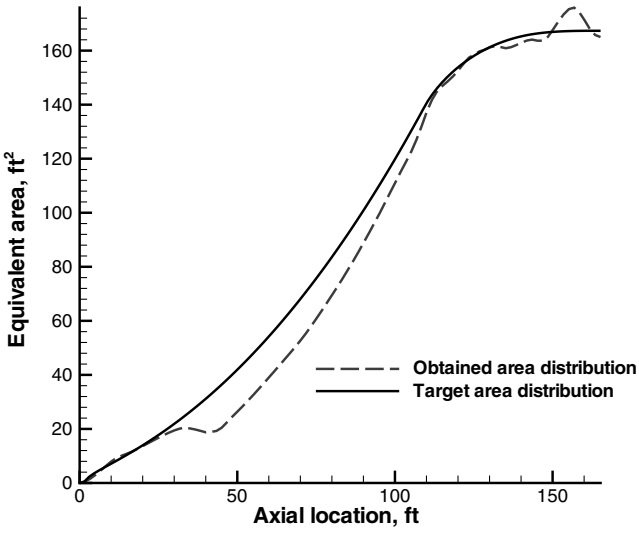

Fig. 23 Comparison of total equivalent areas after nose area matching.

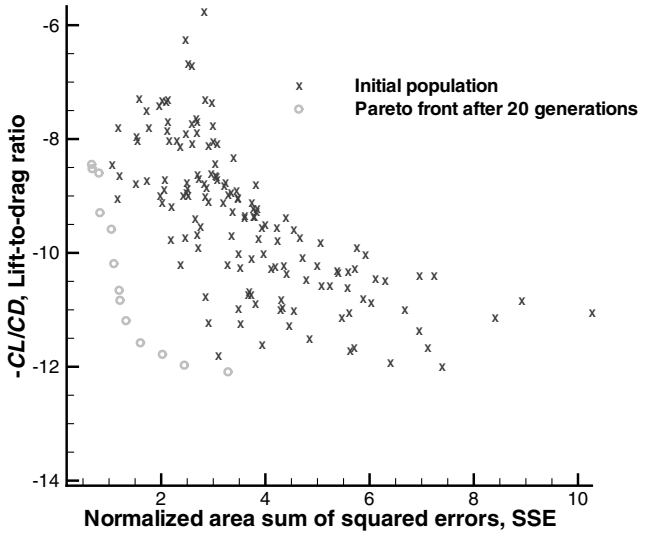

Fig. 24 Pareto front after perturbing wing and tail geometries.

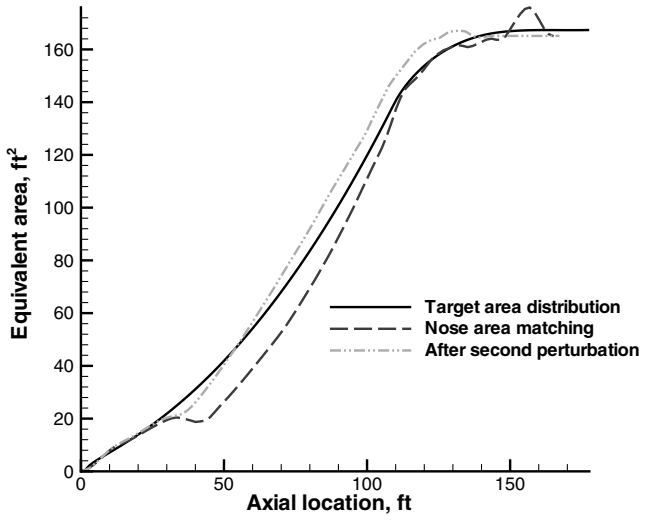

Fig. 25 Comparison of final total equivalent areas.

shape, the other components of the aircraft are altered in order to achieve the target area distribution from step 1. Figure 24 depicts the nondominated individuals after 20 generations. By changing the wing and tail parameters while maintaining the nose shape as obtained from the previous step, the lift-to-drag coefficient increases slightly. The equivalent area distributions are then compared by choosing a point from the nondomination front. Figure 25 shows the comparison of the equivalent areas for a point on the nondominated front. It can be observed from this figure that by changing the geometric parameters of components other than the fuselage, a fairly close area distribution can be obtained. Figure 26 shows four views of one of the best configurations obtained after 20 generations. It can be seen that this configuration has a swept-forward T-tail and multisection wing. This configuration has nacelles under the wing and, using the linearized tool nacelle modification [33], this configuration might have slightly increased boom loudness compared with the same configuration with nacelles over the wing. This nacelle placement effect is not captured in the inverse design procedure, because the objective is not to minimize the perceived loudness, but to achieve a target equivalent area distribution. Thus, there is no bias toward nacelle-over-wing designs in the inverse design procedure.

Although a visually good match is obtained in terms of the area distribution, the F-function and the pressure signature do not match well with the targets. Figure 27 shows the comparison of the near-field effects in terms of the F-functions. As can be seen, because of deviations in the area distribution, the obtained F-function no longer has the shape of the desired target distribution. New wiggles are introduced due to the changes in the second derivative in the area distribution. It has been observed that the near-field signature is extremely sensitive to the total equivalent area distribution [34]. Because the target F-function is not obtained, the ground pressure signature is also different from the target. Figure 28 compares the calculated ground signature with the target signature. The area and pressure signature matching differences can be attributed to the choice of aggressive loudness target and the corresponding equivalent area distribution. Reduction of the vast configuration design space has been achieved while obtaining aircraft shapes that produce equivalent area distributions in the vicinity of the target curve. The area distribution discrepancies, which exist after the conceptual phase, may be overcome by performing shape perturbations over reduced-space geometries in the later stages of design, whereas using nonlinear analyses, wing reflexing, fillets, fairings, and other advanced methods, an exact match of the area distribution as well as ground pressure signature may be obtained.

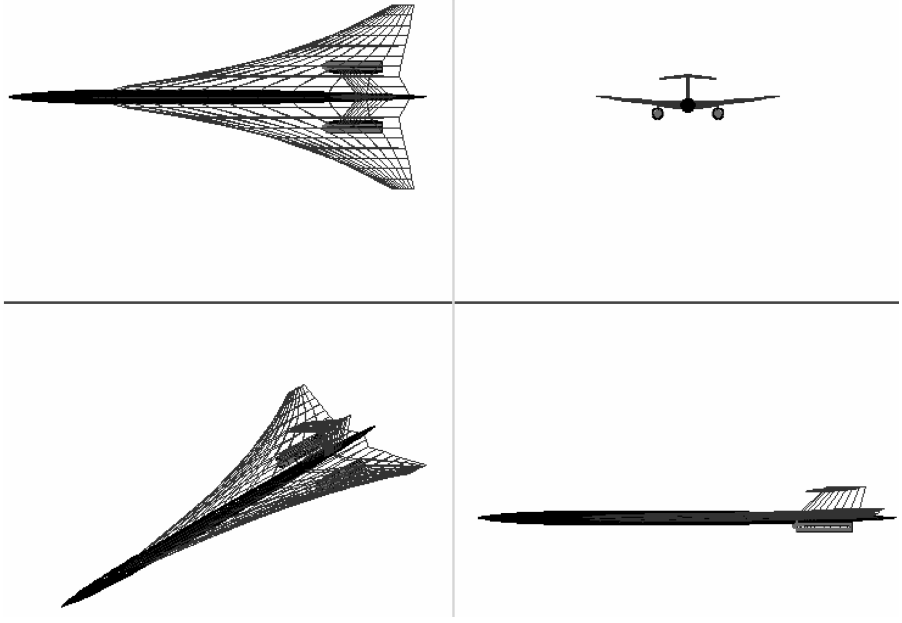

Fig. 26 Four-view sketch of one of the best designs in the design space examined.

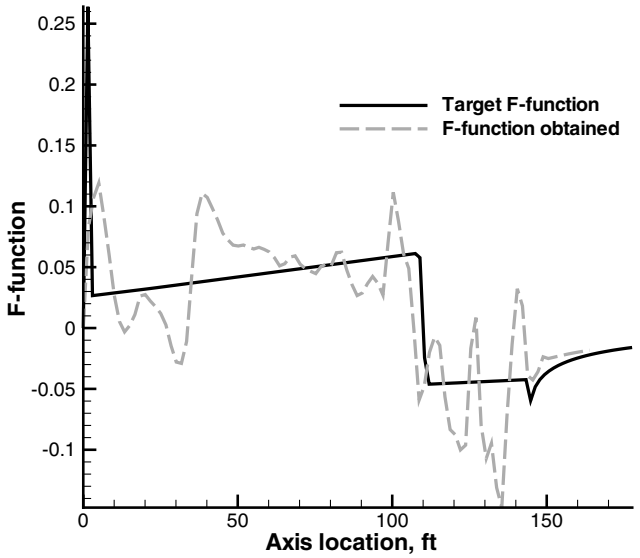

Fig. 27 Comparison of F-functions.

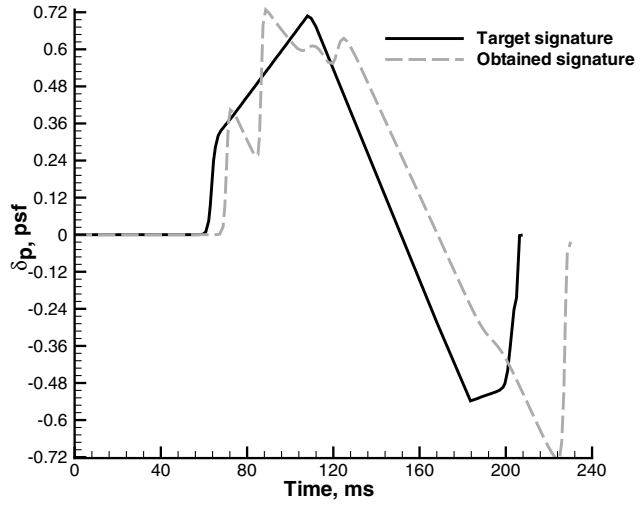

Fig. 28 Comparison of ground signatures.

VII. Conclusion

A new design methodology has been introduced for sonic boom minimization based on improved linearized methods. The geometry generation and discretization procedure enables an efficient and automatic way to combine linearized and nonlinear analysis. The well-accepted SGD equations have been generalized to yield near-field signatures with better far-field characteristics. The relevant equations for this generalization were derived. The shape optimization procedure in conjunction with parallel genetic algorithms allows the designer to explore vast design spaces quickly and efficiently. The probabilistic propagation provides a strategy to include atmospheric fluctuations into the aircraft design process. The bilevel procedure not only serves as a pseudoinverse technique but also induces design flexibility by separating the near- and far-field analysis. With this basic framework, various important studies could be conducted to aid the designer in the conceptual design stages.

It is to be noted that the sonic boom analysis and design conducted in this paper is limited to conceptual aircraft design purposes only. The reason for this is that realistic sonic boom signatures on the ground can be significantly modified and magnified or completely smeared due to gusts, vortical disturbances, thermal/entropy perturbations, or turbulence. This is a complicated dynamical phenomenon that requires much more advanced analysis. For a complete presentation of these advanced features, interested readers must refer to several experimental [35,36], numerical, and theoretical studies [37–39] on these issues. Furthermore, aircraft design for sonic boom minimization may include interactions with the water surface [40,41] during flight over the oceans. These effects have to be considered in the subsequent stages of design.

Acknowledgements

This work was supported under grant NAG-1-02023, "Design Methodology for Revolutionary Aerospace Concepts," from NASA Langley Research Center with Craig Nickol as the technical monitor. We would like to express our sincere thanks to Suraj Unnikrishnan for help with the neural network architecture implementation. Michael Buonanno's help with the geometry generator is greatly appreciated.

References

[1] Mavris, D. N., and Delaurentis, D., "Methodology for Examining the Simultaneous Impact of Requirements, Vehicle Characteristics, and Technologies on Military Aircraft Design," *22nd Congress of the International Council on the Aeronautical Sciences*, International Council of the Aeronautical Sciences, Harrogate, England, U.K., Aug. 2000.

[2] Darden, C. M., "The Importance of Sonic Boom Research in the Development of Future High Speed Aircraft," *Journal of the NTA*, Vol. 65, No. 3, 1992, pp. 54–62.

[3] Henne, P. A., "Case for Small Supersonic Civil Aircraft," *Journal of Aircraft*, Vol. 42, No. 3, May 2005, pp. 765–774.

[4] Rallabhandi, S. K., and Mavris, D. N., "An Unstructured Wave Drag Code for Preliminary Design of Future Supersonic Aircraft," AIAA Paper 2003-3877, 2003.

[5] Rallabhandi, S. K., and Mavris, D. N., "Sonic Boom Minimization Using Improved Linearized Tools and Probabilistic Propagation," AIAA Paper 2005-1019, 2005.

[6] Rallabhandi, S. K., and Mavris, D. N., "Sonic Boom Modelling Under Atmospheric Uncertainty," AIAA Paper 2004-4650, 2004.

[7] Nadarajah, S. K., Jameson, A., and Alonso, J. J., "Sonic Boom Reduction Using an Adjoint Method for Wing-Body Configurations in Supersonic Flow," AIAA Paper 2002-5547, 2002.

[8] Farhat C., Maute, K., and Nikbay, M., "A Shape Optimization Methodology for Reducing the Sonic Boom Initial Pressure Rise," AIAA Paper 2002-145, 2002.

[9] Howe, D. C., "Sonic Boom Reduction Through the Use of Non-Axisymmetric Configuration Shaping," AIAA Paper 2003-929, 2003.

[10] Howe, D. C., "Engine Placement for Sonic Boom Mitigation," AIAA Paper 2002-148, 2002.

[11] Seebass, R., and George, A., "Sonic Boom Minimization," *Journal of the Acoustical Society of America*, Vol. 51, No. 2C, Feb. 1972, pp. 686–694.

[12] Darden, C., "Sonic Boom Minimization with Nose-Bluntness Relaxation," NASA Langley Research Center, TP-1348, Hampton, VA, Sept. 1979.

[13] Morgenstern, J. M., "F-5 Shaped Sonic Boom Demonstrators Persistence of Boom Shaping Reduction Through Turbulence," AIAA Paper 2005-12, 2005.

[14] Whitham, G., "The Flow Pattern of a Supersonic Projectile," *Communications on Pure and Applied Mathematics*, Vol. 5, 1952, pp. 301–347.

[15] Jones, L. B., "Lower Bounds for the Pressure Jump of the Bow Shock of a Supersonic Transport," *The Aeronautical Quarterly*, Vol. 21, Feb. 1970, pp. 1–17.

[16] George, A. R., and Seebass, R., "Sonic Boom Minimization Including Both Front and Rear Shocks," *AIAA Journal*, Vol. 9, No. 10, 1969, pp. 2091–2093.

[17] George, A., and Plotkin, K. J., "Sonic Boom Waveforms and Amplitudes in a Real Atmosphere," *AIAA Journal*, Vol. 7, No. 10, Oct. 1969, pp. 1978–1981.

[18] Vanderplaats, G. N., *Numerical Optimization Techniques for Engineering Design*, 3rd ed., Vanderplaats Research and Development, Colorado Springs, CO, 1999.

[19] Morgenstern, J. M., "Wind Tunnel Testing of a Sonic Boom Minimized Tail-Braced Wing Transport Configuration," AIAA Paper 2004-4536, 2004.

[20] Mack, R. J., "A Supersonic Business-Jet Concept Designed for Low Sonic Boom," NASA Langley Research Center, TM-2003-212435, Hampton, VA, Oct. 2003.

[21] Plotkin, K. J., "PCBoom3 Sonic Boom Prediction Model, Version 1.0c," Wyle Research Labs., Rept. AFRL-HE-WPTR-2001-0155, Arlington, VA, May 1996.
[22] Haykin, S., *Neural Networks: A Comprehensive Foundation*, Pearson Prentice Hall, Upper Saddle River, NJ, 1999.
[23] Anon., *Neural Network Toolbox User's Guide*, MathWorks, Natick, MA, 2002.
[24] Bass, H. E., Raspet, R., Chambers, J. P., and Kelly, M., "Modification of Sonic Boom Wave Forms During Propagation from the Source to the Ground," *Journal of the Acoustical Society of America*, Vol. 111, No. 1, Jan. 2002, pp. 481–486.
[25] Pierce, A. D., and Maglieri, D. J., "Effects of Atmospheric Irregularities on Sonic Boom Propagation," *Journal of the Acoustical Society of America*, Vol. 51, No. 2C, Feb. 1972, pp. 702–721.
[26] Stephens, M., "EDF Statistics for Goodness of Fit and Some Comparisons," *Journal of the American Statistical Association*, Vol. 69, Sept. 1974, pp. 730–737.
[27] Stephens, M., "Goodness of Fit for the Extreme Value Distribution," *Biometrika*, Vol. 64, No. 3, 1977, pp. 583–588.
[28] Mahfoud, S. W., "Niching Methods for Genetic Algorithms," Illinois Genetic Algorithms Laboratory, Rept. 95001, Urbana, IL, May 1995.
[29] Gondra, I., and Samadzadeh, M. H., "A Coarse-Grain Parallel Genetic Algorithm for Finding Ramsey Numbers," *Symposium on Applied Computing*, Association for Computing Machinery, New York, 2003, pp. 2–8.
[30] De Toro, F., Ortega, J., and Diaz, A., "PSFGA: A Parallel Genetic Algorithm for Multiobjective Optimization," *Proceedings of the 10th Euromicro Workshop on Parallel, Distributed and Network-Based Processing*, Institute of Electrical and Electronics Engineers, New York, June 2002, p. 384.
[31] Deb, K., Pratap, A., Agarwal, S., and Meyarivan, T., "A Fast and Elitist Multi-Objective Genetic Algorithm: NSGA-2," Indian Inst. of Technology Kanpur, KanGAL Rept. 200001, Kanpur, India, 2000.
[32] Seebass, R., and Argrow, B., "Sonic Boom Minimization Revisited," *Proceedings of the 2nd Theoretical Fluid Mechanics Meeting*, AIAA, Reston, VA, June 1998.
[33] Mack, R. J., "A Numerical Method for Evaluation and Utilization of Supersonic Nacelle-Wing Interference," NASA Langley Research Center, TN D-5057, Hampton, VA, Feb. 1969.
[34] Rallabhandi, S. K., "Sonic Boom Minimization Through Vehicle Shape Optimization and Probabilistic Acoustic Propagation," Ph.D. Thesis, Georgia Institute of Technology, School of Aerospace Engineering, Atlanta, GA, May 2005.
[35] Lipkens, B., and Blackstock, D. T., "Model Experiment to Study Sonic Boom Propagation Through Turbulence. Part 1: General Results," *Journal of the Acoustical Society of America*, Vol. 103, No. 1, Jan. 1998, pp. 148–158.
[36] Lipkens, B., "Model Experiment to Study Sonic Boom Propagation Through Turbulence. Part 3: Validation of Sonic Boom Propagation Models," *Journal of the Acoustical Society of America*, Vol. 111, No. 1, Jan. 2002, pp. 509–519.
[37] Crow, S., "Distortion of Sonic Bangs by Atmospheric Turbulence," *Journal of Fluid Mechanics*, Vol. 37, Part 3, 1969, pp. 529–563.
[38] Plotkin, K. J., and George, A., "Propagation of Weak Shock Waves Through Turbulence," *Journal of Fluid Mechanics*, Vol. 54, Part 3, 1972, pp. 449–467.
[39] Bass, H. E., Layton, B., Bolen, L., and Raspet, R., "Propagation of Medium Strength Shock Waves Through the Atmosphere," *Journal of the Acoustical Society of America*, Vol. 82, No. 1, 1987, pp. 306–310.
[40] Rochat, J. L., and Sparrow, V. W., "A Computational Analysis of Sonic Booms Penetrating a Realistic Ocean Surface," *Journal of the Acoustical Society of America*, Vol. 109, No. 3, Mar. 2001, pp. 899–908.
[41] Cheng, H., Lee, C., and Edwards, J., "Sonic-Boom Generated Sound Field Under a Wavy Air-Water Interface: Analyses for Incident N Waves," *Journal of the Acoustical Society of America*, Vol. 118, No. 4, Oct. 2005, pp. 2201–2209.